MODELING, IDENTIFICATION AND CONTROL, 1982, VOL. 3, NO. 4, 231–242

doi:10.4173/mic.1982.4.4

A model for solving the Maxwell quasi-stationary equations in a three phase electric reduction furnace

S. EKRANN† and T. SIRA‡

Keywords: *Maxwell's quasi-stationary equations, electric and magnetic fields, three-dimensional, numerical methods, finite differences, staggered grid, electric reduction furnace.*

A computer code has been developed for the approximate computation of electric and magnetic fields within an electric reduction furnace. The paper describes the numerical methods used to solve Maxwell's quasi-stationary equations, which are the governing equations for this problem. The equations are discretized by a staggered grid finite difference technique. The resulting algebraic equations are solved by iterating between computations of electric and magnetic quantities. This 'outer' iteration converges only when the skin depth is larger or of about the same magnitude as the linear dimensions of the computational domain. In solving for electric quantities with magnetic quantities being regarded as known, and vice versa, the central computational task is the solution of a Poisson equation for a scalar potential. These equations are solved by line successive overrelaxation combined with a rebalancing technique.

1. Introduction

The quasi-stationary approximation to Maxwell's equations can be applied to alternating current (a.c.) problems in linear media. Computation of a.c. fields are somewhat more problematic than the corresponding d.c. problem. In the a.c. case, the electric field is influenced by the magnetic induction. One therefore needs to solve the equations for both of these fields. Furthermore, the interaction between the two fields tends to give the solution steeper gradients than in the d.c. case. A.c. fields have been studied in connection with eddy current problems. Most of these studies are limited to two-dimensional problems (Chari 1973, Salon *et al.* 1981). Carpenter (1977) presents a discussion of various formulations of the full three-dimensional problem in terms of vector and scalar potentials. Our formulation differs from these in that the electric current and magnetic flux density fields are kept as the fundamental variables. The coupling between those fields are then treated explicitly in the numerical agorithm.

In order to study the a.c. distribution inside electric reduction furnaces, we have developed a computer program named EROS. This is an acronym for the Norwegian equivalent to 'Electric Reduction Furnace Simulation'. Some computational results from EROS were presented in Ekrann *et al.* (1980). The present paper describes the numerical methods used to solve the field equations in the furnace volume.

Received 15 June 1982.

† Rogalandsforskning, Stavanger, Norway.

‡ Institutt for energiteknikk, Kjeller, Norway.

This work was done at the Institute for Energy Technology for Elkem-Spigerverket and Norsk Jernverk with financial support from the Norwegian Technical and Scientific Research Foundation.

The main geometrical features of an electric reduction furnace are shown in Fig. 1. Three cylindrical electrodes are symmetrically positioned in the furnace pot, which is partly filled with liquid metal and surrounded by a cylindrical iron mantel. 3 phase electric current (50 Hz) is supplied through the electrodes.

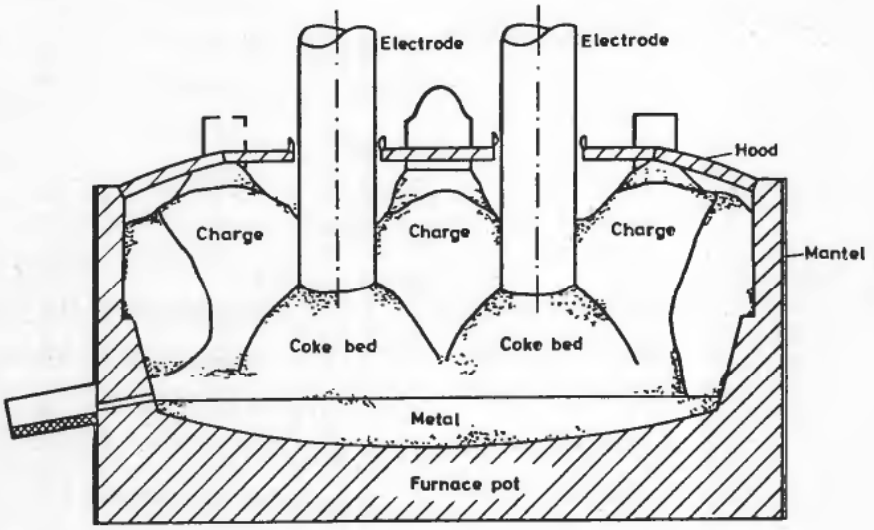

Figure 1. Cross section of electric reduction furnace.

The electric conductivity and the magnetic permeability vary several orders of magnitude over the furnace volume. Electric conductivities typically range from 10^4 S/m in the electrode and 10^2 S/m in the coke bed to 10^{-5} S/m in the cold upper charge. The central part will not be magnetic because of the high temperatures. In the hood and the mantel there may be magnetic materials with a relative permeability in the order of 10^2.

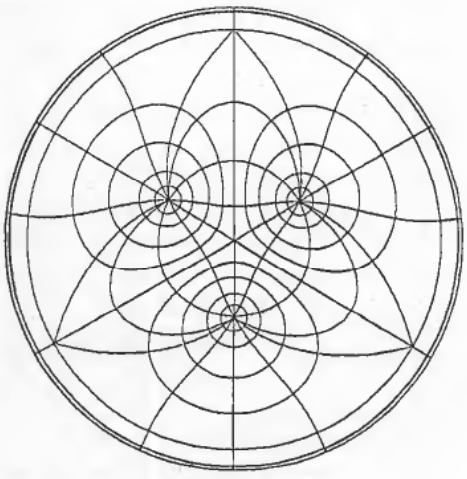

Figure 2. Horizontal coordinate system.

In order to describe the geometry adequately, a special coordinate system was constructed. The vertical coordinate is Cartesian, whereas the horizontal coordinates are curvilinear. The horizontal coordinate system is shown in Fig. 2, where the indicated lines are lines of constant coordinates. The system consists of three deformed cylindrical systems (obtained by conformal mapping) surrounded by an ordinary cylindrical system. The total system is therefore orthogonal except at a few singular points. For ease of presentation, the following exposition will assume Cartesian coordinates.

2. Governing equations

The quasi-stationary approximation to Maxwell's equations are obtained (Weizel 1963) from the full set of Maxwell's equations by deleting the displacement current term. We also assume linear and isotropic media, i.e. linear relationships between the magnetic flux density and the magnetic field strength and between the electric field and the current density. The resulting equations will therefore be linear. We require the boundary conditions to have harmonic time dependence. Because of the linearity, the solution will then also be harmonic. When removing the harmonic time dependence, we arrive at the following equations, written in the SI system of units:

$$\nabla \boldsymbol{J} = 0 \tag{1 a}$$

$$\nabla \times (\boldsymbol{J}/\sigma) = -i\omega \boldsymbol{B} \tag{1 b}$$

$$\nabla \boldsymbol{B} = 0 \tag{1 c}$$

$$\nabla \times (\boldsymbol{B}/\mu) = \boldsymbol{J} \tag{1 d}$$

Here

$i = (-1)^{1/2}$

ω = angular frequency	[1/s]
σ = electric conductivity	[S/m]
μ = magnetic permeability	[H/m]
$\boldsymbol{J}$ = current density (complex vector)	[A/m^2]
$\boldsymbol{B}$ = magnetic flux density (complex vector)	[T]

In eqn. (1) the wave solutions are lost. This is a good approximation since the typical wavelengths are several orders of magnitude larger than the linear dimensions of the computational domain. Also, capacitance effects are excluded. At the power frequency these effects are negligible in the present problem.

The assumption of linear media, on the other hand, limits the usefulness of the model somewhat. For example, real furnaces contain materials which exhibit magnetic hysteresis. Also, in some types of furnaces there are electric arcs extending from the bottom of the electrodes. At present, these effects are ignored.

Scaling

We define a set of new (primed) quantities through

$$\left.\begin{aligned} \boldsymbol{r} &= L^* \boldsymbol{r}' \quad \text{(radius vector)} \\ \sigma(\boldsymbol{r}) &= \sigma^* \sigma'(\boldsymbol{r}') \\ \mu(\boldsymbol{r}) &= \mu^* \mu'(\boldsymbol{r}') \end{aligned}\right\} \tag{2}$$

and

$$\left.\begin{aligned} \boldsymbol{J}(\boldsymbol{r}) &= \frac{1}{L^*}\,\boldsymbol{J}'(\boldsymbol{r}') \\ \boldsymbol{B}(\boldsymbol{r}) &= \mu^*\boldsymbol{B}'(\boldsymbol{r}') \end{aligned}\right\} \tag{3}$$

L^*, σ^* and μ^* are constants with the dimensions of $\boldsymbol{r}$, σ and μ, respectively. They are understood to be typical values for these quantities. Using eqns. (2) and (3) we get from eqn. (1):

$$\nabla' \boldsymbol{J}' = 0 \tag{4 a}$$

$$\nabla' \times (\boldsymbol{J}'/\sigma') = -i\omega L^{*2}\mu^*\sigma^*\boldsymbol{B}' \tag{4 b}$$

$$\nabla' \boldsymbol{B}' = 0 \tag{4 c}$$

$$\nabla' \times (\boldsymbol{B}'/\mu') = \boldsymbol{J}' \tag{4 d}$$

Equation (4) contains only scale independent quantities except for the factor

$$\eta = \omega L^{*2}\mu^*\sigma^* = L^{*2}/\delta^{*2}$$

where

$$\delta^* = (\omega\mu^*\sigma^*)^{-1/2}$$

is a typical skin depth. η, a squared relative length, is the critical parameter of the problem. Roughly speaking, η governs the form of the solution. Also, this parameter is of great importance for the performance of the numerical solution procedure we are using.

Boundary conditions

Equation (1) is solved in a bounded three-dimensional domain. As indicated in Fig. 2, the domain is cylindrical. Radially the domain is large enough to include the mantel and vertically the domain includes the hood and terminates at the metal surface. For $\boldsymbol{B}$ we always use the component normal to the boundary ($\boldsymbol{B}_\perp$) as the boundary condition. Since very little is known about $\boldsymbol{B}_\perp$ in practical situations, it has been set equal to zero in all calculations so far. For $\boldsymbol{J}$ we use $\boldsymbol{J}_\perp = 0$ as a boundary condition on the vertical boundary and on the top boundary outside the intersection with the electrodes. For the lower boundary and the electrode intersection boundary, either $\boldsymbol{J}_\perp$ or the component of $\boldsymbol{J}$ parallel to the boundary, $\boldsymbol{J}_\parallel$, is used as a boundary condition. Figure 3 illustrates the four possible alternatives. In practical situations, $\boldsymbol{J}$ is not known at the metal surface. However, because of the very high electrical conductivity, the metal bath effectively acts as a short-circuit. Therefore $\boldsymbol{J}_\perp = 0$ can be used on the lower boundary if a thin slice of the metal is included into the computational domain (Figs. 3 (*a*), 3 (*c*)). The short-circuiting effect is alternatively achieved by using $\boldsymbol{J}_\parallel = 0$ at the metal surface (Figs. 3 (*b*), 3 (*d*)). Figures 3 (*c*) and 3 (*d*) show the two alternatives we get when $\boldsymbol{J}_\parallel$ is used instead of $\boldsymbol{J}_\perp$ on the electrode intersections. Here we have more than one area where $\boldsymbol{J}_\parallel$ is given. This means that the boundary conditions for $\boldsymbol{J}$ have to be supplemented by voltage conditions. A voltage drop is defined as the line integral of $\boldsymbol{E} \equiv \boldsymbol{J}/\sigma$ along a specified path between two points. The paths that are used are indicated by the dashed lines in Figs. 3 (*c*), 3 (*d*). The voltage drop along these paths must be specified. Note that these apparently

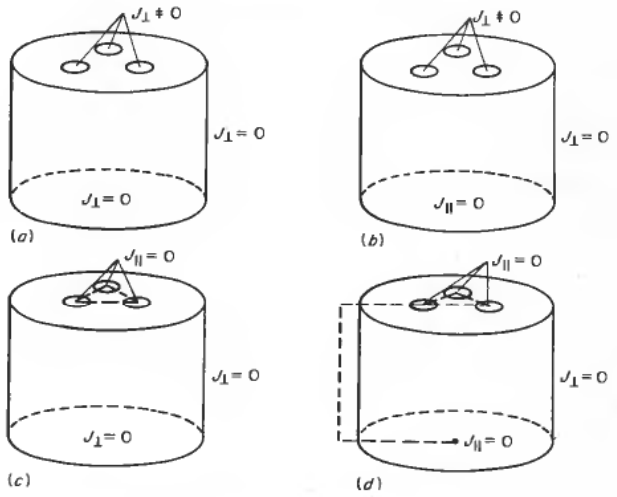

Figure 3. Boundary conditions for $\boldsymbol{J}$.

homogeneous cases, the boundary forcing is produced only by the specified voltage drops. How the voltage drop conditions are actually implemented, are described in somewhat more detail later.

3. Solution strategy

The governing equations (1) can be divided into two subsystems. When $\boldsymbol{B}$ is known, (1 *a*, *b*) can be used to solve for $\boldsymbol{J}$. Correspondingly, (1 *c*, *d*) can be solved for $\boldsymbol{B}$ when $\boldsymbol{J}$ is known. This property is utilized in our solution scheme. We compute $\boldsymbol{J}$ and $\boldsymbol{B}$ alternately in an iterative fashion. This is called the 'outer iteration'. In the actual implementation, real and imaginary parts of $\boldsymbol{J}$ and $\boldsymbol{B}$ are treated separately. The computational sequence is Re $\boldsymbol{J}\rightarrow$Re $\boldsymbol{B}\rightarrow$Im $\boldsymbol{J}\rightarrow$Im $\boldsymbol{B}$.

Convergence of outer iteration

The solution of (4 *a*, *b*) can be written formally

$$\boldsymbol{J}' = F_J(-i\eta \boldsymbol{B}') + \boldsymbol{H}_J$$

or, due to linearity,

$$\boldsymbol{J}' = -i\eta F_J(\boldsymbol{B}') + \boldsymbol{H}_J \tag{5}$$

Here, $F_J(-i\eta \boldsymbol{B}')$ is the solution to (4 *a*, *b*) with homogeneous boundary conditions. $\boldsymbol{H}_J$ is the solution when the source term $(-i\eta \boldsymbol{B}')$ vanishes. Correspondingly, (4 *c*, *d*) have the solution

$$\boldsymbol{B}' = F_B(\boldsymbol{J}') + \boldsymbol{H}_B \tag{6}$$

Using (5) and (6) iteratively and eliminating $\boldsymbol{B}'$, we have

$$\boldsymbol{J}'^{n+1} = -i\eta(F_J F_B)(\boldsymbol{J}'^n) - i\eta F_J(\boldsymbol{H}_B) + \boldsymbol{H}_J \tag{7}$$

where n is the iteration count. When letting $\boldsymbol{J}'$ be the solution to (4) and defining the error $\boldsymbol{D}^n$ as

$$\boldsymbol{D}^n = \boldsymbol{J}' - \boldsymbol{J}'^n$$

we arrive at

$$D^n=(-i\eta)^n(F_JF_B)^n(D^o) \tag{8}$$

We conclude that η is of paramount importance for the convergence of the outer iteration even in the continuous case, although nothing quantitative can be said until the properties of the mapping (F_JF_B) have been established. Equation (8) implies a slower convergence of (7) when η increases.

Treatment of the subsystems

The subsystems (1 *a*, *b*) and (1 *c*, *d*) have an identical form. We describe the treatment of (1 *a*, *b*) when $\boldsymbol{B}$ is regarded as known. Equation (1 *c*, *d*) is treated in an analogous manner.

$\boldsymbol{J}$ is decomposed into

$$\boldsymbol{J}=\boldsymbol{J}_1+\boldsymbol{J}_2 \tag{9}$$

with $\boldsymbol{J}_1$ satisfying

$$\nabla\times(\boldsymbol{J}_1/\sigma)=-i\omega\boldsymbol{B} \tag{10}$$

implying

$$\nabla\times(\boldsymbol{J}_2/\sigma)=0$$

or

$$\boldsymbol{J}_2=-\sigma\nabla\phi \tag{11}$$

where ϕ is a scalar potential. Equations (9), (11) and (1 *a*) give

$$\nabla(\sigma\nabla\phi)=\nabla\boldsymbol{J}_1 \tag{12}$$

Equation (10) has an infinite number of solutions. The choice of solution may be based on the ease of implementation. The numerical solution of (12) is the main computational task of the present problem. The boundary conditions for $\boldsymbol{J}$ transform into boundary conditions for $\boldsymbol{J}_2$ when $\boldsymbol{J}_1$ is given. A particular solution for $\boldsymbol{J}_1$ is always computed before solving for ϕ. $\boldsymbol{J}_\perp$ given corresponds to a von Neuman type of boundary condition for ϕ

$$\frac{\partial\phi}{\partial n}=\frac{1}{\sigma}(\boldsymbol{J}_{1\perp}-\boldsymbol{J}_\perp)$$

$\boldsymbol{J}_\parallel$ given is equally straightforward. Let $\partial\Omega_i(i=1, N)$ be the simply connected parts of the boundary $\partial\Omega$ where $\boldsymbol{J}_\parallel$ is given as a boundary condition. In each $\partial\Omega_i$ we have:

$$\phi_i(\boldsymbol{r})=\phi_i(\boldsymbol{r}_0)+\int_C\frac{1}{\sigma}(\boldsymbol{J}_1-\boldsymbol{J}_\parallel)d\boldsymbol{l} \tag{13}$$

where $d\boldsymbol{l}$ is the length element along the arbitrary curve $C\in\partial\Omega_i$ connecting $\boldsymbol{r}_0\in\partial\Omega_i$ and $\boldsymbol{r}\in\partial\Omega_i$. Thus, when $\boldsymbol{J}_\parallel$ is given it corresponds to a Dirichlet type of boundary condition for ϕ.

The voltage conditions described earlier fix all but one of the constants $\phi_i(\boldsymbol{r}_0)$. The last constant may be chosen arbitrarily, as its value does not influence the primary variable $\boldsymbol{J}$. For von Neuman conditions on the whole boundary, the potential must be specified at one internal point. The value chosen here does not influence $\boldsymbol{J}$.

4. Discretization

In the standard fashion, the computational domain is divided into a three-dimensional array of grid cells by a set of constant coordinate surfaces. We assume constant material data (σ and μ) within each cell. A staggered grid is used, that is the computational points for the magnetic quantities are displaced half a grid increment in each of the three coordinate directions as compared to the computational points for electric quantities. This is illustrated below for an internal grid cell with space indices i, j and k. Arrows on the grid cell edges indicate components of $\boldsymbol{J}$, while arrows on the cell face centres indicate components of $\boldsymbol{B}$. The crosses indicate computational points for the scalar potential in (12), while the small circle indicates a computational point for the corresponding magnetic scalar potential. Equation (12) is discretized by what is commonly referred to as box integration. For each grid cell corner the equation is integrated over a control volume, or box, centred at the grid cell corner and extending halfway into the neighbouring grid cells. Through Gauss' theorem the volume integral is transformed into a surface integral over the control volume boundary. A typical contribution is the surface integral from a cell face normal to the x-direction

$$\int\int \sigma\left(E_{1x}-\frac{\partial\phi}{\partial x}\right) dy\, dz \tag{14}$$

where $\boldsymbol{E}_1 = \boldsymbol{J}_1/\sigma$.

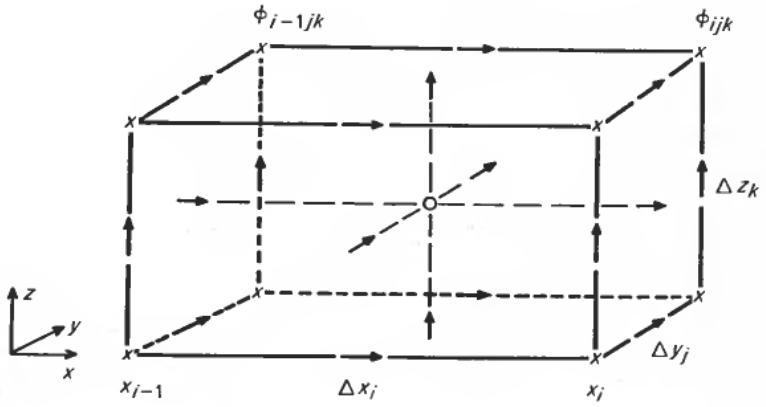

Figure 4. Computational points.

The integral represents the current through this face. For the face common to the boxes centred on ϕ_{i-1jk} and ϕ_{ijk} in Fig. 4, (14) is approximated by

$$\frac{\phi_{i-1jk}-\phi_{ijk}+V_{xijk}{}^{J}}{\Delta x_i}\int\int \sigma\, dy\, dz \tag{15}$$

with

$$V_{xijk}{}^{J} = \int_{x_{i-1}}^{x_i} E_{1x}\, dx$$

where the line integral is taken along the appropriate grid cell edge. The surface integral in (15) can be evaluated exactly when σ is a constant within each grid cell.

For each internal box, the contributions from the six faces are assembled, giving an equation expressing current conservation. This is a linear equation in the box potential and the six neighbouring potentials. For a potential on the boundary, the equation must be modified. If $J_\perp$ is given, the corresponding face current is known. When $J_\parallel$ is given, ϕ may be computed from (13), which then replaces the current conservation equation.

The resulting algebraic equations can be written in matrix form as

$$A\phi = b \tag{16}$$

The elements of the vector ϕ are the unknown potentials and the elements of b are the contributions from the source term in (12) and from the non-homogeneous boundary conditions. It can easily be shown that the coefficient matrix A is symmetric and diagonally dominant, implying that (16) may be solved by a standard iterative method like successive line overrelaxation (SLOR).

The preceding is all fairly straightforward, except for the coefficient σ in (12) being discontinuous. This, however, is no problem since we require parallel components of E to be continuous over discontinuities in σ. Equation (15) may be interpreted as a parallel coupling of electric conductances.

The corresponding scalar potential for B is treated in an analogous manner. The control volumes will in this case coincide with the grid cells. The expression equivalent to (15) may be interpreted as a series coupling of magnetic conductances, i.e. we require the normal component of B to be continuous over discontinuities in μ.

With non-varying σ and μ, the approximations described above are second order in grid increments (Δx, Δy, Δz) when these are constant. Where the grid increments change, the approximations are first and zeroth order for the electric and magnetic potentials, respectively (Aziz *et al.* 1979). A local zeroth order approximation is not particularly pleasing, of course, but by no means catastrophic. A first order approximation to the magnetic potential equation can be achieved by using the same computational points for the magnetic as for the electric quantities, abandoning the staggered grid. As we shall see, however, the staggered grid has the benefit of increasing the accuracy of the coupling between the electric and the magnetic quantities.

The equation (10) is discretized by integrating over grid cell faces. For convenience, we may choose $E_{1z}=0$. Using Stoke's theorem for the back face of the box in Fig. 4 as an example, we get:

$$V_{xijk}{}^{J} - V_{xijk-1}{}^{J} = -i\omega \int\int B_y \, dx \, dz \tag{17}$$

Note first that there are no approximations involved in the terms on the left hand side. Also, these quantities are exactly the ones needed in (15) and in the implementation of $J_\parallel$ boundary conditions. Note also that an approximation to the integral on the right hand side is directly available from the solution of the magnetic equation equivalent to (16), which expresses the magnetic flux conservation.

The discretization described above can be seen as approximating a differential equation problem with a three-dimensional network problem. An elementary cell of the network is shown in Fig. 5. A three-dimensional electric network staggered with a three-dimensional magnetic network is shown. The conductances, as described previously, are computed from σ and μ, together with the geometrical quantities.

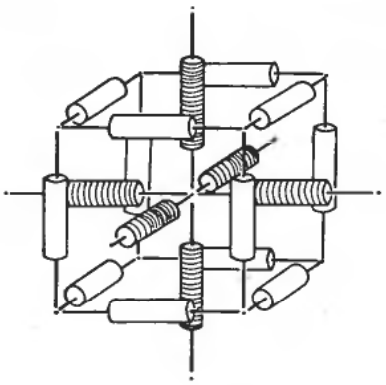

Figure 5. Three-dimensional staggered electric and magnetic networks.

Accuracy of coupling between electric and magnetic quantities

Consider the simple example of an infinite conducting wall (σ, μ constant) with

$$\boldsymbol{J}=J(x)\boldsymbol{k} \quad \text{and} \quad \boldsymbol{B}=B(x)\boldsymbol{j}$$

where $\boldsymbol{k}$ and $\boldsymbol{j}$ are unit vectors in z- and y-directions, respectively (see Fig. 6). Equation (1) reduces to

$$\frac{\partial J}{\partial x}=i\omega\sigma B \tag{18 a}$$

$$\frac{\partial B}{\partial x}=\mu J \tag{18 b}$$

With boundary conditions

$$J(x=0)=J_0 \quad J(x=\infty)=0$$

(18) has the solution

$$J(x)=J_0 \exp\left(-(i\omega\sigma\mu)^{1/2}x\right)$$

At the discrete points $x_k=k\Delta x$, $k=0, \ldots$, we have

$$J(k\Delta x)=J_0(\exp\left(-(i\eta^*)^{1/2}\right))^k\equiv J_0 a^k$$

with

$$\eta^*=\omega\sigma\mu\Delta x^2$$

Discretizing (18) in a uniform staggered grid, as indicated in Fig. 6 we get

$$\frac{J_{k+1}-J_k}{\Delta x}=i\omega\sigma B_{k+1} \quad k=0, \ldots$$

$$\frac{B_{k+1}-B_k}{\Delta x}=\mu J_k \qquad k=1, \ldots$$

which after the elimination of B can be solved to give

$$J_k=J_0\left(\frac{2+i\eta^*-\sqrt{(\eta^*(4i-\eta^*))}}{2}\right)^k\equiv J_0 b^k \tag{19}$$

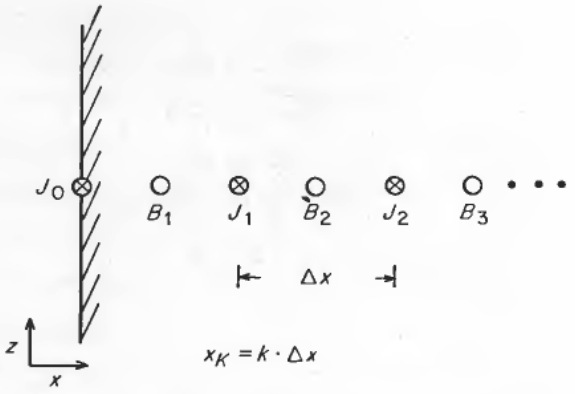

Figure 6. Grid for one-dimensional equations.

Similarly, with a non-staggered grid (requiring interpolation) we can compute the discrete solution

$$J_k = J_0 \left(\frac{2-\sqrt{(i\eta^*)}}{2+\sqrt{(i\eta^*)}} \right)^k \equiv J_0 c^k \tag{20}$$

The accuracy of the approximations (19) and (20) is determined by the accuracy with which b and c, respectively, approximate a.

It can be proved that $|b|$, like $|a|$, tends monotonically to zero as η^* tends to infinity, while $\lim_{\eta^* \to \infty} |c| = 1$. The η^* dependence of $|a|$, $|b|$ and $|c|$ is shown in the Table. From the Table is is obvious that the staggered grid approximation is superior to the non-staggered one. We expect this conclusion to be valid in the general three-dimensional case as well and this is our reason for the choice of a staggered grid.

η^*	10^{-4}	10^{-2}	10^{-1}	10	10^2
$\|a\|$	0·99295	0·93173	0·7996	0·1069	$8{\cdot}493 \times 10^{-4}$
$\|b\|$	0·99295	0·93170	0·7989	0·0972	$9{\cdot}997 \times 10^{-3}$
$\|c\|$	0·99295	0·93179	0·8011	0·4694	$7{\cdot}566 \times 10^{-1}$

Accuracy of staggered and non-staggered grid approximations.

5. Solution of the discrete equations

Solution of the curl equations

The solution of the curl equations (17) is straightforward. If $V_{xijk}{}^J$ is known at the lower boundary (17) may be solved recursively. Since $B_z = 0$ here, we may choose $E_{1x} = E_{1y} = V_{xij0}{}^J = V_{yij0}{}^J = 0$.

In the magnetic case, the equation equivalent to (17) can be solved in the same manner, except that the first $V_x{}^B$, $V_y{}^B$ are computed in a horizontal plane $\Delta z_1/2$ over the lower boundary. We may never assume $J_z = 0$ here. However, $V_x{}^B$ and $V_y{}^B$ can easily be constructed to satisfy the proper curl equation, even with $J_z \neq 0$, providing a starting point for the recursion. We will omit the details.

Solution of potential equations

As mentioned previously, the coefficient matrix A in (16) has the properties which guarantee convergence when using the SLOR technique. We use SLOR as our basic scheme. SLOR, however, as well as other standard point or block iterative techniques, will have a disastrously slow convergence in the present case. This is caused by the occurrence of isolated subdomains with a very high conductivity. Combining SLOR with a rebalancing technique (Nakamura 1977, Froehlich 1967) we achieve dramatic improvements. This technique has previously been used by De la Valee Poussin (1968) on a similar problem.

Convergence of the outer iteration in the discrete case

In the discrete case, the mappings F_J and F_B in eqns. (5)–(8) will be matrices. From (8) we may immediately conclude that the outer iteration will converge if

$$\eta\rho(F_J F_B) < 1$$

where $\rho(F_J F_B)$ is the spectral radius of $F_J F_B$.

In the general case it is difficult to estimate the eigenvalues of $F_J F_B$. In order to get some quantitative idea when to expect convergence, we resort once more to a one-dimensional example.

One-dimensional example

The geometry of the example is as illustrated in Fig. 6, except that the wall has finite thickness. J is given at both end points with the values J_0 and J_{K+1}, respectively. The outer iteration takes the form

$$\boldsymbol{C}\boldsymbol{I}^{n+1} = i\eta^* \boldsymbol{I}^n + \boldsymbol{F} \tag{21}$$

with

$$\boldsymbol{C} = \begin{bmatrix} -2 & 1 & & & 0 \\ 1 & -2 & 1 & & \\ & \ddots & \ddots & \ddots & \\ & & 1 & -2 & 1 \\ 0 & & & 1 & -2 \end{bmatrix} \quad \boldsymbol{I} = \begin{bmatrix} J_1 \\ \vdots \\ J_K \end{bmatrix} \quad \boldsymbol{F} = \begin{bmatrix} -J_0 \\ 0 \\ \vdots \\ 0 \\ -J_{K+1} \end{bmatrix}$$

C has the eigenvalues (Isaacson and Keller 1966)

$$\lambda_p = -4 \sin^2 \left(\frac{\pi}{2} p/K+1 \right) \quad p = 1, \ldots, K$$

from which we conclude that (21) converges if

$$\frac{\eta^*}{4 \sin^2 \left(\frac{\pi}{2} \Big/ K+1 \right)} < 1 \tag{22}$$

$|i\eta^* \lambda_1^{-1}|$ being the spectral radius of $i\eta^* C^{-1}$.

For fixed η^* the left hand side of (22) is larger the larger K is, i.e. the convergence properties of (21) deteriorates with increasing wall thickness. The same thing happens with decreasing skin depth $\delta=(\omega\mu\sigma)^{-1/2}$. This agrees with the general conclusions.

Writing

$$\frac{\eta^*}{4\sin^2\left(\frac{\pi}{2}\Big/K+1\right)}=\frac{\eta\left(\frac{\Delta x}{L}\right)^2}{4\sin^2\left(\frac{\pi}{2}\frac{\Delta x}{L}\right)}$$

where $L=(K+1)\Delta x$ is the wall thickness and $\eta=\omega\sigma\mu L^2$, we have in the limiting case with L constant and $\Delta x\to 0$ the convergence criterion

$$\frac{\eta}{\pi^2}<1 \tag{23}$$

At the other extreme, $L=2\Delta x$, we have

$$\frac{\eta}{8}<1 \tag{24}$$

Roughly speaking, (23) and (24) express that convergence in the outer iteration is to be expected when the skin depth is larger than about a third of the linear dimensions of the problem. The convergence depends only weakly on the fineness of discretization. This implies that we may have a discretization which is sufficiently accurate but for which the outer iteration fails to converge.

Practical experience indicates that these conclusions are valid even in the three-dimensional case when the computational domain is approximately homogeneous. In the present problem we have subdomains (electrodes, hood, mantel), where the skin depth is several orders of magnitude smaller than elsewhere. Therefore, these subdomains are decisive for the convergence of the outer iteration.

References

Aziz, K., and Settari, A. (1979). *Petroleum Reservoir Simulations* (Applied Science Publishers), pp. 75–80.

Carpenter, C. J. (1977). Comparison of alternative formulations of 3-dimensional magnetic-field and eddy-current problems at power frequencies, Proc. IEE, Vol. 124, No. 11, pp. 66–74.

Chari, M. V. K. (1973). Finite element solution of the eddy current problem in magnetic structures, IEEE paper T 73 320-9.

Ekrann, S., Holmelid, A., and Torp, T. (1980). A three-dimensional mathematical model for electromagnetic quantities in three phase electric reduction furnaces, *9th International Congress of Electroheat*, Cannes 1980.

Froehlich, R. A. (1967). A theoretical foundation for coarse mesh variational techniques, GA-7870, General Atomic, San Diego, California.

Isaacson, E., and Keller, H. W. (1966). *Analysis of Numerical Methods* (John Wiley & Sons), p. 456.

Nakamura, S. (1977). *Computational Methods in Engineering and Science* (John Wiley & Sons), pp. 285–327.

Salon, S. J., Schneider, J. M., and Uda, S. (1981). Boundary element solutions to the eddy current problem, Proc. of the 3rd international seminar on boundary element methods, Springer Verlag, pp. 14–25.

De la Valee Poussin, F. (1968). An accelerated relaxation algorithm for iterative solution of elliptic equations, Siam J. Numer. Anal, Vol. 5, No. 2, pp. 340–351.

Weizel, W. (1963). *Lehrbuch der Theoretischen Physik* (Springer-Verlag), pp. 400–403.